Effect of critical zone annealing time on mechanical properties, microstructure, and elemental distribution of Fe-0.21C-10Mn-4.8Al-0.5Cu-0.4Cr-0.2Ti medium manganese steel

Xinghui Li[1] , Cainian Jing[1]* , Tao Lin[1], Yingming Tu[1], Hengbin Liu[1], Can Peng[1], Jidong Zhang[1], Xinyu Yang[1]

[1]*School of Materials Science and Engineering, Shandong Jianzhu University, 1000 Fengming Road, Licheng District, Jinan, Shandong 250101, P. R. China*

Abstract

This paper investigates the effects of intercritical annealing time on the mechanical properties, microstructure, and element distribution of Fe-0.21C-10Mn-4.8Al-0.5Cu-0.4Cr-0.2Ti medium manganese steel by setting different intercritical annealing times in the critical zone. The mechanisms underlying the observed phenomena were analyzed using characterization methods, including tensile testing, hardness testing, X-ray diffraction (XRD), scanning electron microscopy (SEM), and electron backscatter diffraction (EBSD). The results show that the material exhibits a tensile strength of 1250 MPa, an elongation of 45 %, and a strength-ductility product as high as 56.3 GPa%. The optimal microstructure is a complex phase structure composed primarily of austenite with multiple morphologies, δ-ferrite, and martensite. With the prolongation of annealing time, the morphology of retained austenite gradually transforms from fine lath-shaped to larger block-shaped austenite. The thermodynamic and mechanical stability of retained austenite in the AT40 sample is significantly improved, thereby enhancing the mechanical properties of the sample.

K e y   w o r d s: intercritical annealing, complex phase, stability of retained austenite

1. Introduction

With the increasing demand for automotive lightweighting and safety performance, the optimization of the strength-ductility product of advanced high-strength steels has become the focus of research in the field of materials [1]. Medium-Mn Steel (MMS) is considered a candidate for the third generation of advanced high-strength steels due to its excellent mechanical properties and cost advantages. The core design concept is to regulate austenite stability via intercritical annealing, thereby reconciling martensitic phase-transition-induced plasticity (TRIP effect) with twinning-induced plasticity (TWIP effect) and achieving synergistic enhancement of strength and plasticity. However, the stability of austenite is highly dependent on chemical composition, grain size, and elemental partitioning behavior. The mechanisms by which annealing process parameters (e.g., annealing time) regulate the evolution of multiphase organization and elemental diffusion kinetics remain to be explored in depth.

Existing studies have shown that the partitioning of austenite-stabilizing elements, such as C and Mn, is decisive for the phase composition during annealing in the critical zone [2]. However, for medium manganese steel systems containing multiple alloying elements (e.g., Al, Cu, Ti), the diffusion behavior of these elements and their effects on interfacial migration and precipitate phase formation remain unclear. In particular, the addition of Al elements may promote δ-ferrite formation while inhibiting carbide precipitation, while the introduction of trace elements such as Cu and Ti may affect dislocation motion and phase

*Corresponding author: e-mail address: jcn@sdjzu.edu.cn

Table 1. Chemical element compositions and phase transformation temperature points of the experimental materials (wt.%)

C	Mn	Cu	Al	Ti	Cr	Bal.	Ac_1	Ac_2	M_s
0.21	10	0.52	4.8	0.24	0.39	Fe	657.7	811.5	180.3

transition kinetics through grain boundary deviation or nano-precipitated phases. The complexity of this multi-component system makes the mechanism underlying the correlation between microstructural evolution and mechanical properties still controversial [3–8].

In this study, the influence of critical-zone isothermal annealing time on the multiphase organization and morphology, austenite stability, and elemental distribution is systematically investigated in Fe-0.21C-10Mn-4.8Al-0.5Cu-0.4Cr-0.2Ti medium-manganese steel. Through the design of gradient annealing time experiments, combined with tensile mechanical testing, microhardness analysis, X-ray diffraction (XRD) and scanning electron microscope (SEM) characterization, the following key scientific issues are analyzed: (1) how the annealing time drives the transformation of austenite from a fine lath-like to a bulk-like morphology and affects its thermodynamic and mechanical stability; (2) the diffusion paths of multiphase alloying elements (Al, Cu, and Ti) and their influence on the interfacial stability of austenite and phase transition resistance during the annealing process.

2. Materials and methods

2.1. Materials

In this experiment, Fe-0.21C-10Mn-4.8Al-0.5Cu-0.4Cr-0.2Ti medium manganese steel was used as the research object, and its specific chemical composition is shown in Table 1.

The austenite transition temperature (Ac_1) and the end transition temperature (Ac_3) during heating of medium manganese steels are important parameters in determining the annealing process. To derive the phase transition temperature points of the test steels in this study, the organizational transition temperatures of the test steels at thermodynamic equilibrium, calculated according to the empirical equations [9–11], are shown in Table 1, where the empirical equations are shown below:

$$Ac_1 = 739.3 - 22.8 \times C - 6.8 \times Mn + 18.2 \times Si + 11.7 \times Cr - 15 \times Ni - 6.4 \times Mo - 5 \times V - 28 \times Cu, \quad (1)$$
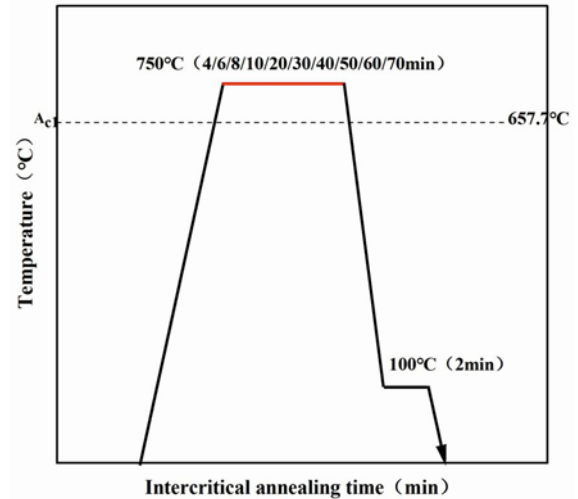

Fig. 1. Machining process roadmap with different annealing times.

$$Ac_3 = 957.3 - 224.5 \times C0.5 - 17 \times Mn + 34 \times Si - 14 \times Ni + 21.6 \times Mo + 41.8 \times V - 20 \times Cu, \quad (2)$$

$$Ms = 692 - 502 \times (C + 0.86 \times N)0.5 - 37 \times Mn - 14 \times Si + 20 \times Al - 11 \times Cr. \quad (3)$$

As shown in Table 1, the phase transition temperatures of the tested steels range from 657.7 to 811.5 °C. The martensitic phase transition temperature of the tested steels is 180.3 °C.

2.2. Hot rolling and heat treatment

Firstly, the steel is melted in a vacuum induction furnace and subsequently forged into billets. Next, the billets are heated to 1300 °C and held in a homogeneous austenitic state for 2 hours. Subsequently, multiple passes of hot rolling were performed to produce 4 mm-thick hot-rolled sheets. In the hot-rolling process, the initial rolling temperature is set at 1200 °C, and the final rolling temperature is maintained at 1000 °C. After the hot rolling is completed, the plates are pickled. Subsequently, the hot-rolled sheets are annealed at 750 °C for 5 hours. After annealing, they are cooled to room temperature using air. Finally, the plate thickness was reduced to 1.5 mm by cold rolling to meet the target.

After obtaining the target plate, a standard heat-treated tensile specimen was machined from the steel plate using a DK7735 molybdenum wire EDM cutter in accordance with ASTM E8.

According to the heat-treatment processing roadmap shown in Fig. 1, the cut specimens were subjected to heat-treatment tests, and the overall process consisted of critical-zone annealing followed by fractionation.

Specifically, based on a large number of previous experiments, using the MXQ1700 high-temperature chamber atmosphere furnace and selecting 750 °C as the annealing temperature, orthogonal experiments were conducted, setting 4, 6, 8, 10, 20, 30, 40, 50, 60, and 70 min as the variables, and after the end of the annealing holding time, the fractionation treatment was carried out at a holding time of 100 °C for 2 min. To ensure the accuracy of the experimental data, three specimens were processed at each annealing holding time, and the best specimens were selected and labeled AT4, AT6, AT8, AT10, AT20, AT30, AT40, AT50, AT60, and AT70. Finally, the appropriate data were selected and averaged for the stretched specimens at each temperature.

2.3. Tensile test

After heat treatment, the test steel is subjected to a tensile test using a universal testing machine (Model: WDW-100E) at room temperature. Before tensile testing, the test steel should be polished. The test distance is 25 mm, the tensile rate is controlled at $1 \, \text{mm} \, \text{min}^{-1}$, and the Test software is used to record tensile data in detail.

2.4. Microstructural analysis

Characterization of the tensile specimens was performed by first polishing them sequentially with 200#, 400#, 600#, 800#, and 1000# sandpaper, followed by mechanical polishing. The polished test steel was corroded using a 4 vol.% nitric acid alcohol solution, and the treatment was completed when no obvious scratches were observed using a metallurgical microscope.

An X-ray diffractometer (XRD; RIKEN Smart Lab) equipped with a Cu target was used to determine the volume fraction of residual austenite and the phase composition of the test steel, with a scanning speed of $2° \, \text{min}^{-1}$ and a scanning range of $40°–100°$. The volume fraction of residual austenite in the test steel before and after stretching was calculated according to Eq. (4):

$$V_\gamma = 1/[1 + (I_\alpha K_\gamma / I_\gamma K_\alpha)] \times 100 \, \%, \qquad (4)$$

where V_γ represents the volume fraction of residual austenite, I_α refers to the combined intensity of the martensitic diffraction peaks (200) and (211), K_γ is the reflection coefficient of the austenitic phase, I_γ is the austenitic diffraction the combined intensity of peaks (200), (220), and (311), and K_α is the reflection coefficient of the martensitic phase.

To further investigate the influence of different annealing temperatures on the organizational evolution of the test steels, microstructural observations of the

test steels under different annealing times after grinding and polishing corrosion treatment were carried out using field emission scanning electron microscopy (FE-SEM, SUPRATM 55), and the scanning images were subjected to point scanning and line scanning to provide theoretical support for analyzing the elemental distribution as well as the mechanism of elemental movement.

3. Results and discussion

3.1. Microstructural analysis

To analyze the effect of annealing time on the specimen, EBSD analysis was performed, and regions of the specimen before and after stretching were selected for characterization. Figures 2a–c show the EBSD images of the specimen before stretching at annealing times of 6, 40, and 70 min. As shown in Fig. 2, the distribution of grain orientation in the medium manganese steel organization at an annealing time of 6 min was more diffused and disordered, with relatively small differences between grain orientations, and regions of different colors were interspersed. The differently colored regions are interlaced, and there is no discernible tendency toward aggregation or preferential orientation. This indicates that in the initial stage of annealing, atomic mobility is low, and the grains have not grown or undergone orientation adjustment. With an annealing time extended to 40 min, the red (bcc phase) and green (fcc phase) regions exhibit increased aggregation. Some regions of the grains begin to show a tendency of preferential orientation, and some larger grains begin to form. The boundaries between the grains of different orientations gradually become clear. This means that as the annealing time is prolonged, the atomic diffusion is intensified, the grains begin to annex the surrounding small grains and grow up, and at the same time, some of the grains begin to adjust the orientation to reduce the grain boundary energy; when the annealing time reaches 70 min, the green area occupies the dominant position, the grains are obviously coarsened, and the orientation of the grains tends to be concentrated, so that the organization becomes more homogeneous. This indicates that after prolonged annealing, grain growth continues; small-angle grain boundaries gradually disappear, large-angle grain boundaries gradually dominate, and, finally, a more uniform large-grain organization is formed.

Combined with the mechanical property analysis, it can be seen that, before stretching, when the annealing time is short, the grain is fine; at this time, the fcc/bcc ratio is about 1.06. With increasing annealing time, the grain size of medium manganese steel increases. At an annealing time of 40 min, the grain
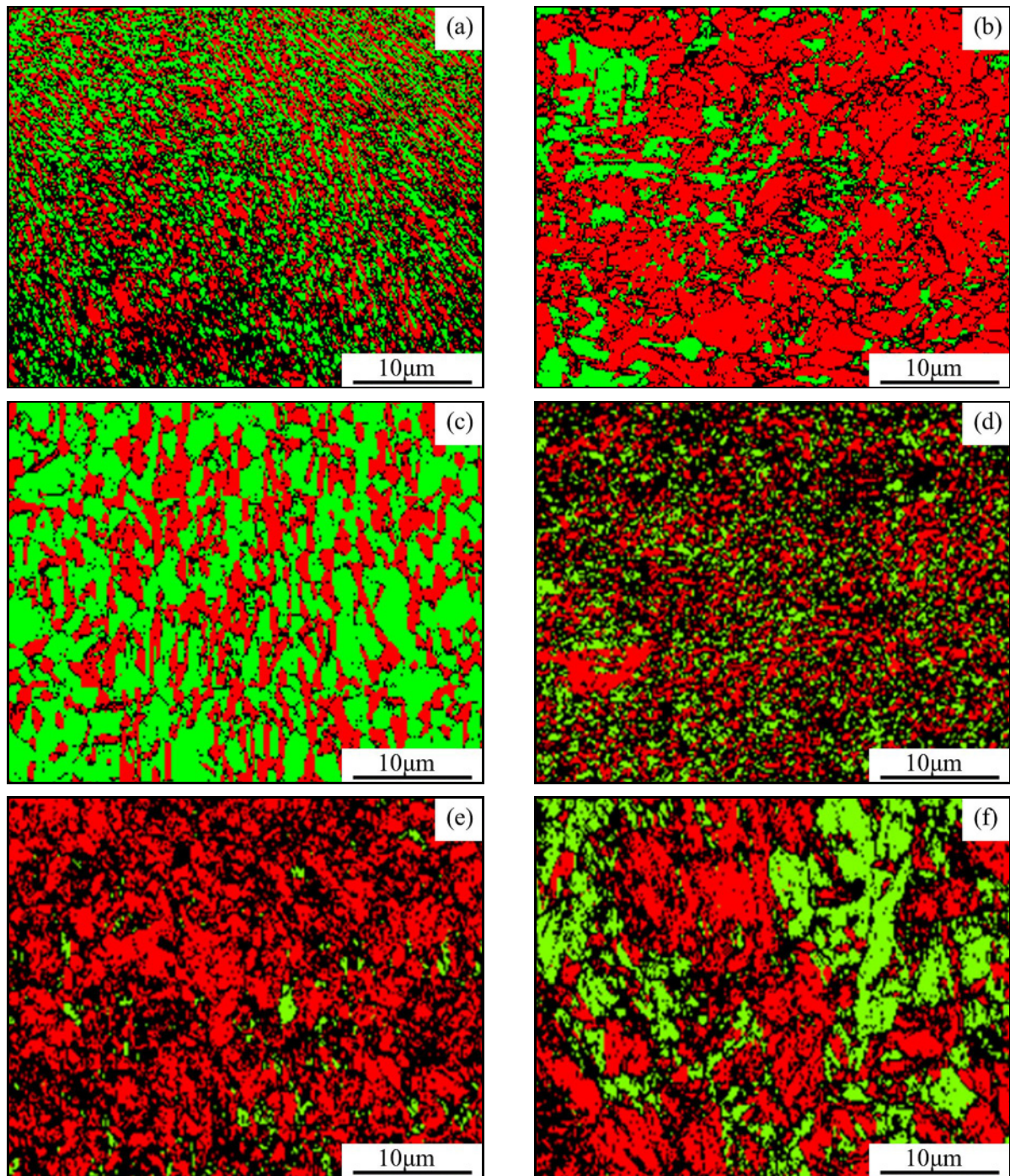
Fig. 2. EBSD images of the specimens under different annealing times, (a)–(c) are EBSD images of the specimens before stretching at annealing times of 6, 40, and 70 min, respectively, and (d)–(f) are EBSD images of the specimens after stretching at annealing times of 6, 40, and 70 min.

exhibits complex phase organization, with an fcc/bcc ratio of approximately 0.25. Under the synergistic effect of multiple phases, the specimen exhibits good overall mechanical properties, and bcc phases predominate during deformation. The soft phase (ferrite) undergoes the first plastic deformation, and the hard phase (martensite) impedes dislocation motion, resulting in significant work hardening that enhances the

material's fatigue resistance and strength. At the same time, the fcc phase, i.e., the stable residual austenite, can be formed through the TRIP or TWIP effects. The fcc phase, i.e., stable residual austenite, can improve the mechanical properties of the specimen through the TRIP or TWIP effect. With the further increase of annealing time, the ratio of fcc/bcc phase is 1.62, which is significantly higher, and the bcc phase is relatively
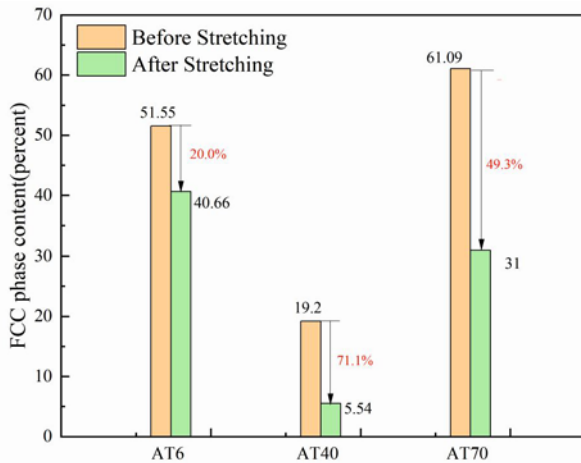
Fig. 3. Volume fraction of fcc phase before and after stretching of the specimens with different annealing times and the conversion ratio.

less, in which the volume fraction of ferrite phase is also relatively less, resulting in the brittleness of the specimen increased by reducing the ductile matrix; at the same time, the fcc phase is much more and more stable, which contributes less to the plastic deformation, resulting in the reduction of the elongation.

To further analyze the specimen after stretching, tissue distribution and changes, EBSD characterization, Figures 2d–f show the annealing times of 6, 40, and 70 minutes after stretching. The organization of the specimen after stretching has obvious changes compared with that before stretching, overall after stretching, the specimen organization is finer, and the residual austenite content changes significantly, combined with the residual austenite conversion rate before and after stretching in Fig. 3. The residual austenite content decreases slightly when the annealing time is 6 min, and the conversion rate of residual austenite reaches 71.1 % when the annealing time is increased to 40 min. Although the residual austenite content before stretching is low, "high quality" residual austenite in the process of tensile TRIP effect occurs in the vast majority of strain-induced martensite, as a hard phase, to improve the strength of the specimen. At the same time, during continuous production of new martensite, greater energy is consumed, thereby delaying necking and fracturing and improving plasticity. Therefore, at this time, the residual austenite content slightly decreased. At this time, the specimen's comprehensive mechanical properties are excellent. With a further increase in annealing time to 70 min, the bcc phase increased significantly, and the tensile strength of the specimen also increased significantly; however, elongation relative to the AT40 specimen decreased. Excessive annealing time leads to grain coarsening. The residual austenite is large but not sufficiently

stable; during tensile deformation, it transforms too quickly into martensite, resulting in reduced plasticity and diminished strong plasticity.

To further analyze the stability of residual austenite, the combined residual austenite conversion rate can be determined by extending the annealing time. The stability of residual austenite shows a pattern of initial decline followed by an increase. AT40 specimens have the highest rate of conversion, indicating that the residual austenite is transformed into martensite to a higher degree, when a very good TRIP effect occurs, and greatly improves the mechanical properties of AT40 specimens.

As shown in Fig. 4, after stretching, the dislocation density of the specimens increased significantly, with standard deviations of 0.63, 0.61, and 0.43 for the AT6, AT40, and AT70 specimens, respectively, before fcc phase stretching. There was a significant increase after stretching, with the standard deviation of AT70 specimens increasing by 0.85. According to the Locus theory, AT70 specimen has the highest residual austenite dislocation density, a large amount of dislocation plugging, which corresponds to a significant increase in tensile strength and a decrease in plasticity; whereas, for AT6 and AT40 specimens, the standard deviation before and after stretching of the fcc phase is lower, but due to the AT6 specimen, the holding time is short, the atomic diffusion capacity is limited, the grain size is small, and the grain boundaries hinder the dislocations from escaping. It results in serious dislocation plugging and stress concentration, and the properties deteriorate. For the AT40 specimen, the grain grows upward. On the other hand, the grain growth and grain size are moderate, while the dislocation density is slightly reduced. The proportion of movable dislocations is increased, which is strengthened by Hall-Petch, and at the same time, dislocations are allowed to slip and coordinate the deformation, to improve the mechanical properties of the specimen.

Figure 5 shows scanning electron microscopy images of the microstructure of medium manganese steel after different annealing times. It is evident that with increasing annealing time, the microstructural features and morphology of Fe-0.21C-10Mn-4.8Al-0.5Cu-0.4Cr-0.2Ti medium manganese steel undergo significant changes.

After annealing, the microstructure of the test steel consists mainly of ferrite, residual austenite, and martensite. Under short annealing times, the austenite morphology is dominated by a fine lath structure, with banded δ-ferrite distributed along the rolling direction, and the organization retains more rolling features, such as deformation bands. With increasing annealing time, the organization gradually undergoes regression recrystallization, the deformation bands decrease, and the organization becomes more homogeneous.
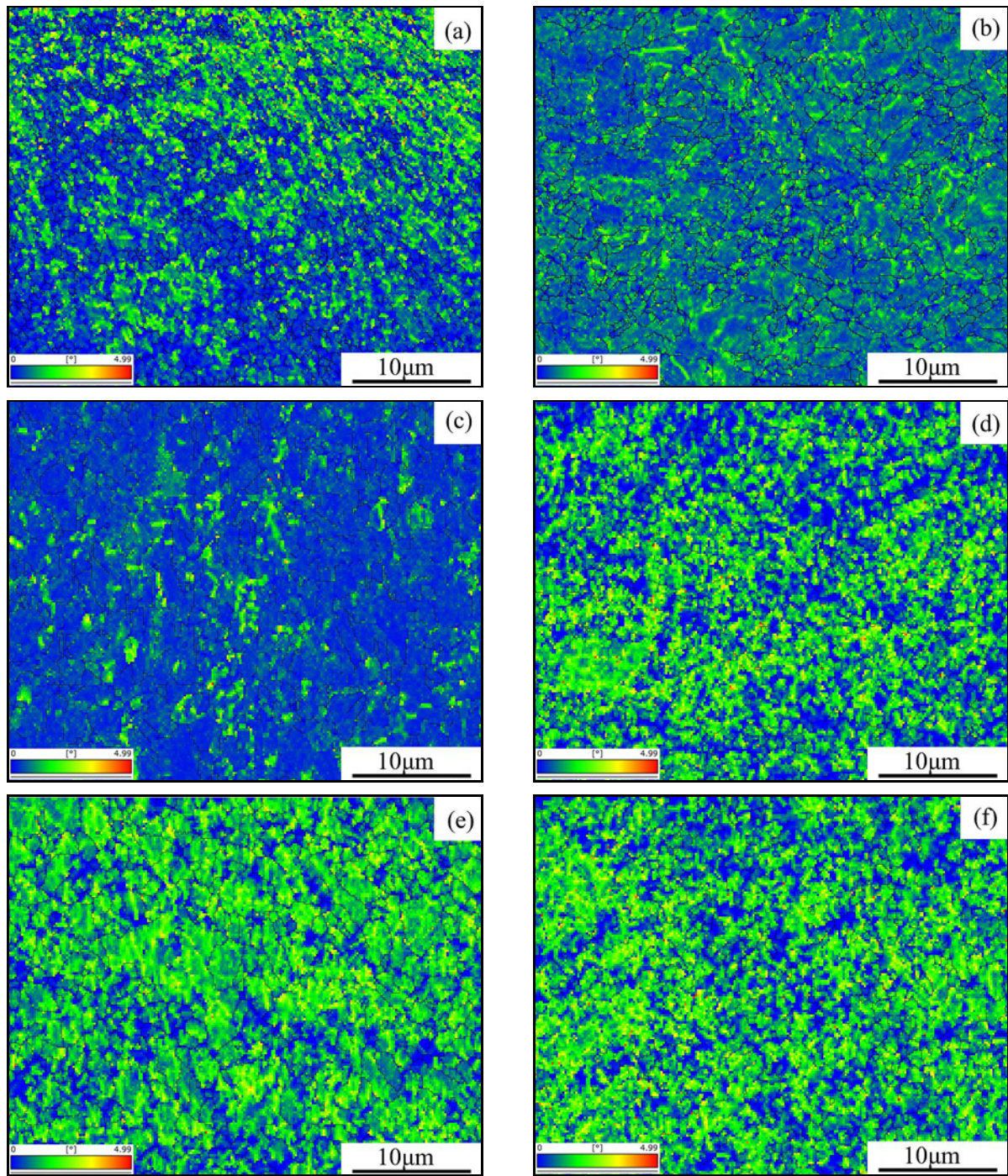
Fig. 4. Statistics of local orientation difference of specimens before and after stretching with different annealing times; before stretching: (a) AT6KAM, (b) AT40KAM, and (c) AT70KAM; after stretching: (d) AT6KAM, (e) AT40KAM, and (f) AT70KAM.

From a grain-scale perspective, it can be observed that at the beginning of the annealing holding period, grain growth begins to occur slowly. With a further increase in annealing time, the grains gradually coarsen.

In general, annealing time significantly affects the grain growth kinetics of medium-manganese steels, and appropriate control of annealing time can achieve the desired grain size and optimize the overall performance of the steel.

mance of the steel.

To observe the evolution of the organization morphology, 6000 electron scanning images of the microstructure of the Mn steel under different annealing times were acquired, as shown in Figs. 6a–e. With increasing annealing time, the microstructural morphology of the Fe-0.21C-10Mn-4.8Al-0.5Cu-0.4Cr-0.2Ti Mn steel has changed significantly.
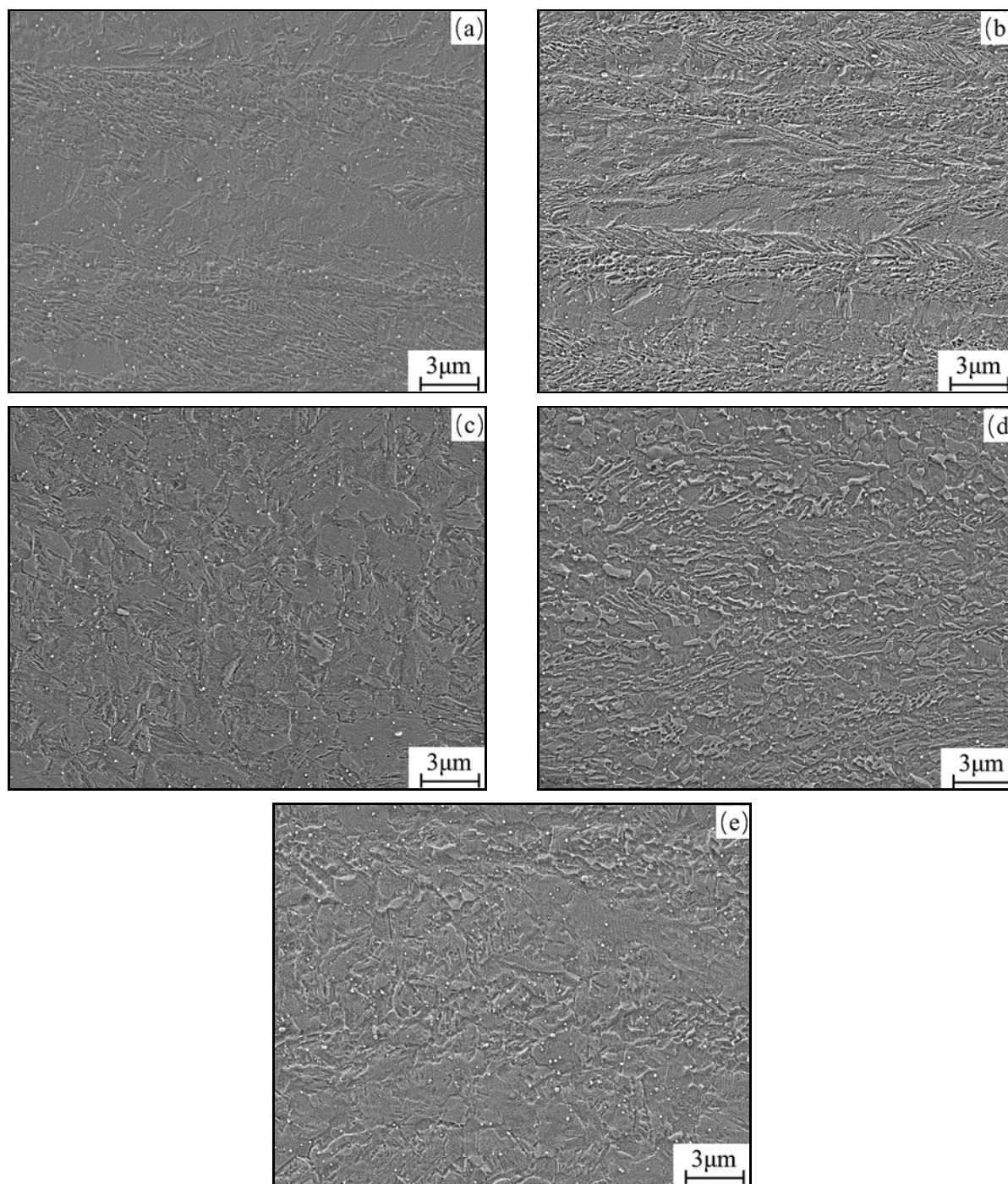
Fig. 5. SEM scanned images of the material at different annealing times, 3000 × ; (a)–(e) annealed for 6, 20, 40, 60, and 70 min.

At a shorter annealing time (Fig. 6a), the organization shows a more lath-like structure and more obvious deformation characteristics. With longer annealing times, the lath-like structure gradually decreases, and the organization becomes more homogeneous and diffuse (Figs. 6b,c). At longer annealing times (Figs. 6d,e), the tissue morphology is more irregular, with larger, more irregularly shaped regions, indicating significant restitution and recrystallization.

As shown in the images, at the beginning of annealing (Fig. 6a), the grains are relatively small and unevenly distributed. With increasing annealing time (Figs. 6b–e), the grains grow gradually; at longer annealing times (Fig. 6e), the grain size increases significantly. The observed trend in grain growth is consistent with the conclusion that longer annealing times promote grain growth and that grain size significantly affects the properties of medium manganese steel, such
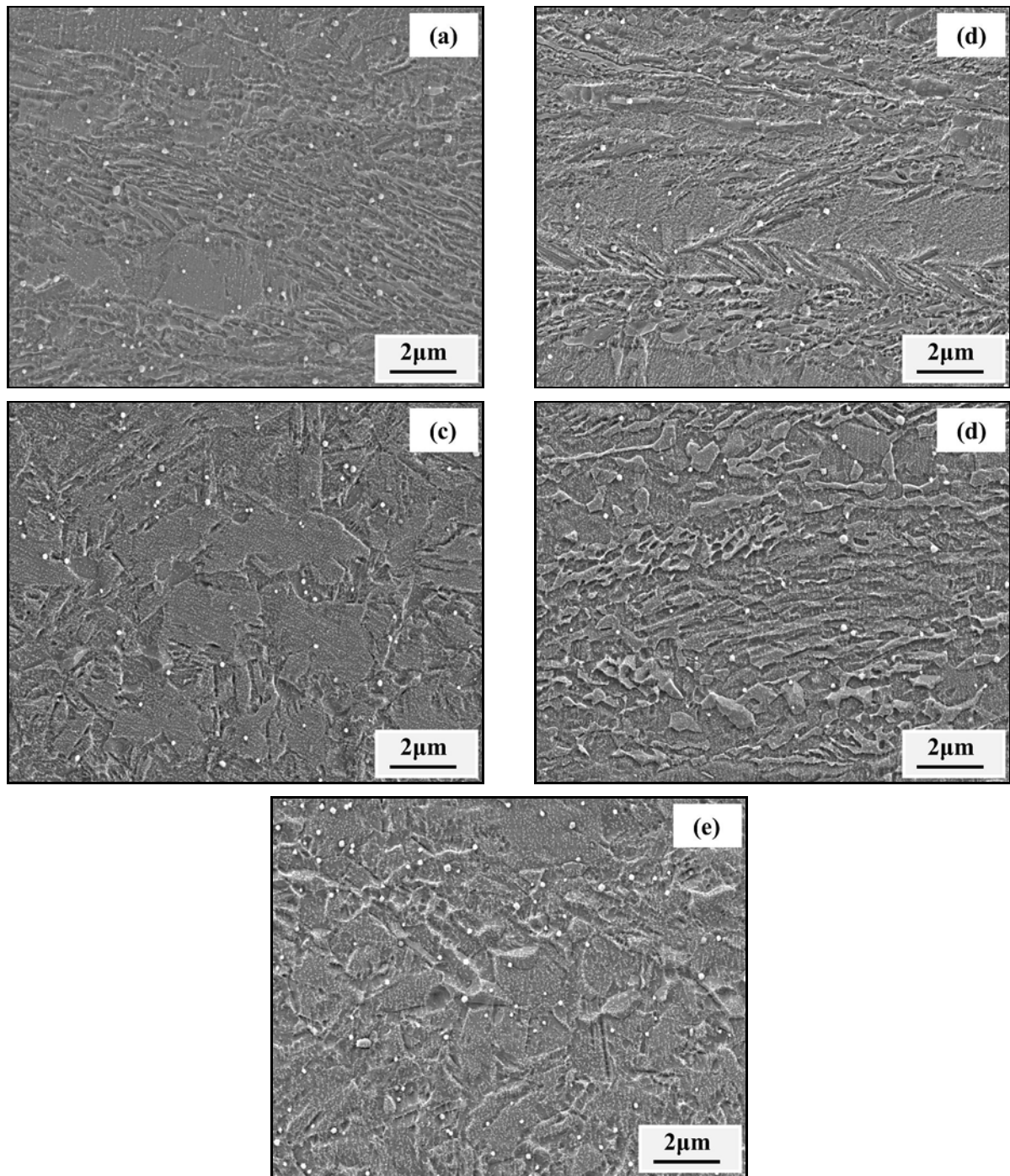
Fig. 6. SEM scanned images of the material at different annealing times, 6000×; (a)–(e) annealed for 6, 20, 40, 60, and 70 min.

as strength and toughness.

At the same time, annealing time affects the phase composition in medium manganese steels, and the content of residual austenite varies with annealing time.

Combined with the work-hardening curve shown in Fig. 12, the transition zone between the tensile and non-tensile regions of the specimen usually corresponds to the yield point of the material, and the yield point is the key point of the material from the elastic point is the key point of the material from the elastic deformation (non-tensile region) to the transition to plastic deformation (tensile region), and its strain is usually 0.2 to 0.5 %, which is the basis for the selection of the tensile region and the non-tensile region. The following XRD analysis is primarily conducted on the specimens' stretched and unstretched regions. Figure 7a is the XRD energy spectrum of the stretching region, and Figure 7b is the XRD energy spectrum of the unstretched portion of the XRD spectrum. In the
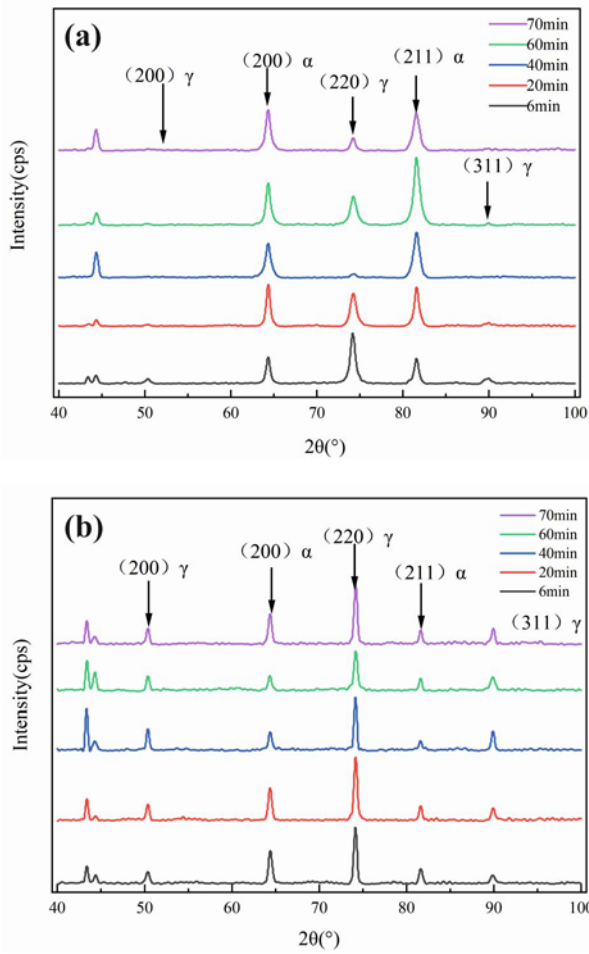
Fig. 7. XRD scanning images of deformed (a) and non-deformed (b) regions at different annealing times.

Fig. 8. Comparison of residual austenite content between deformed (a) and non-deformed (b) areas at different annealing times.

XRD spectrum, clear austenite and martensite peaks are observed, and with increasing annealing time, the diffraction peaks in the area exhibit regular changes.

Figure 8 compares residual austenite content between deformed and non-deformed zones at different annealing times, and the austenite transformation rate before and after stretching. There are small-angle deviations in the diffraction summits of ferrite/martensite and austenite at different annealing times, which may be attributed to the restitution and recrystallization of the grains or lattice distortion during the annealing process. It is observed that, with increasing annealing time, the residual austenite content decreases initially and then increases, in both the stretched and unstretched regions. It is worth noting that the conversion rate of residual austenite during stretching varies with annealing time. With increasing annealing time, the conversion rate first increases and then decreases. When the annealing time is 20 min, the conversion rate reaches 77.1 %. At this time (see Fig. 9), the mechanical stability of the residual austen-
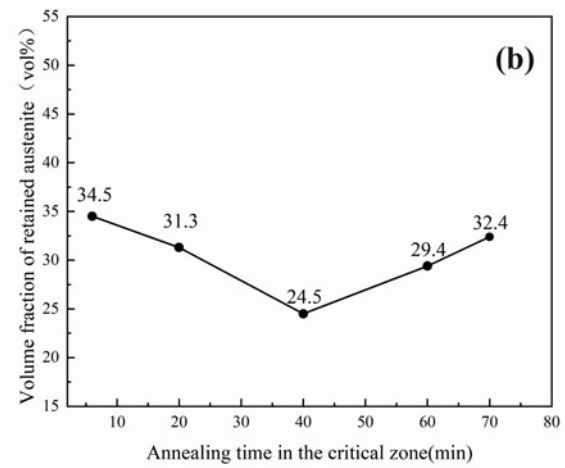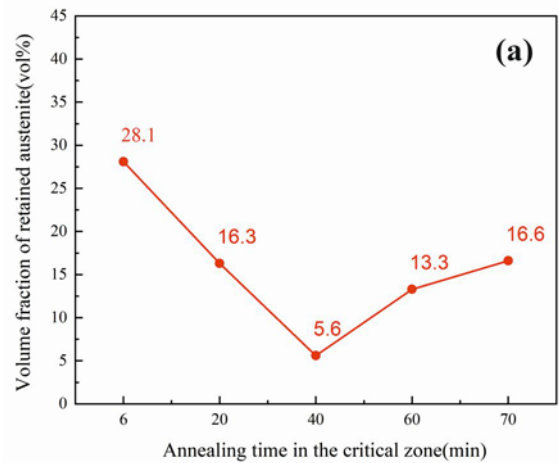
ite is the lowest, and it is more likely to occur in the deformation process of the continuous TIRP effect.

According to Fig. 8b, with the extension of the critical zone annealing time from 10 min to 40 min, the volume fraction of residual austenite in the unstretched part of the medium manganese steel decreases from 34.5 to 24.5 %; when the time is further extended to 70 min, the volume fraction rises back to 32.4 %, which shows a significant trend of "decreasing first and then increasing".

This phenomenon is closely related to the dynamic distribution of carbon and manganese during annealing and to recrystallization behavior.

At the beginning of the critical zone annealing (10–40 min), the diffusion of carbon from austenite to ferrite dominates. According to [12], as the annealing time increases, the migration of carbon leads to a decrease in the carbon content of austenite, its stability, and gradual decomposition into other phases, resulting in a decrease in the volume fraction of residual austenite. The kinetic process of this phase is closely
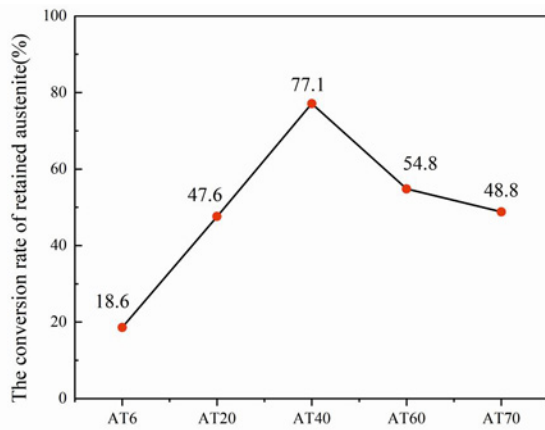
Fig. 9. Residual austenite conversion before and after stretching for different annealing times.

related to the diffusion rate of carbon, and it isn't easy to complete sufficient solute redistribution in a relatively short period of time.

When the annealing time exceeds 40 min, the thermal activation energy of atoms increases, thereby promoting ferrite recrystallization. In-situ TEM observed that the equiaxed ferrite formed by recrystallization provides a new nucleation site for the reverse transformation of austenite [13]. At this time, carbon and manganese elements were re-enriched in austenite by long-range diffusion, resulting in a gradual recovery of their volume fractions. This stage of the austenite regeneration process relies on sufficient annealing time to achieve uniform solute distribution and interfacial migration.

A quantitative comparative analysis of the mechanical stability of the residual austenite can also be performed by using Eq. (5), summarized by Sugimoto et al. [14]:

$$f_{\gamma\varepsilon} = f_{\gamma 0}\exp(-k\varepsilon), \tag{5}$$

where k is the mechanical stability coefficient of residual austenite and $f_{\gamma 0}$ and $f_{\gamma\varepsilon}$ represent the volume fraction of residual austenite (in %) before deformation and at true strain, respectively. It is worth noting that a smaller k value indicates greater mechanical stability of the residual austenite.

By calculating the k-values of 0.74, 2.03, 3.64, 2.02, and 1.75 for the materials with annealing times of 6, 20, 40, 60, and 70 min, respectively, it can be clearly seen that the mechanical stability of the material's residual austenite is the lowest at an annealing time of 20 min.

When the annealing time is 6 min, the volume fraction of residual austenite is higher, reaching 28.1 vol.%, and the mechanical stability is higher, and the conversion rate of residual austenite during

stretching is only 18.6 %. The TRIP effect cannot be fully realized, so the plastic product is less strong. For annealing time 40 min, the volume fraction of residual austenite is very low, only 24.5 vol.%, but the residual austenite conversion rate is 77.1 %, which is with block austenite conversion rate higher, and has a certain relationship (Fig. 9). At this time, austenite large number of growth, resulting in a reduction in the dream content of individual austenite, in the occurrence of strain, can be slowly transformed. The material continues to exhibit sufficient TRIP effect, thereby achieving the highest volume of strong plasticity and good mechanical properties. When the annealing time is greater than 60 min, austenite grows, block austenite reduces, laminated austenite increases, and austenite thermal stability is worse. At this time, the volume fraction of residual austenite is approximately 30 vol.%, and the residual austenite conversion rate is approximately 50 %, which is moderate; however, this is attributable to the point allocation. However, due to the short time, the resulting austenite in the carbon and manganese elements is relatively small, the quality of residual austenite is poor, which will lead to the transformation of residual austenite in the deformation process faster, resulting in larger strain, making it difficult for residual austenite to occur continuously, resulting in the TRIP effect.

3.2. Mechanical properties analysis

With increasing annealing temperature, tensile strength increases, whereas elongation and the strong plastic product first increase and then decrease. With an annealing time of 40 min, the tensile strength reaches 1250 MPa, but the elongation rate decreases. Subsequently, the tensile strength decreases and then rises; the elongation rate and the strong plastic product in the annealing time reach 50 min, at which they attain maximum values of 55.5 % and 61 GPa, respectively.

It can be inferred from the mechanical property plots at different annealing times (Fig. 10) that multiple factors influence the fluctuations in properties as the annealing holding time increases, and further characterization and analysis are needed to provide a more precise explanation of the underlying mechanisms.

As shown in Fig. 11, the annealing time varies across the stress-strain curves of the test steels; with increasing annealing time, elongation first increases and then decreases. The overall trend in annealing temperature is lower, and the tensile curve appears to exhibit a more pronounced yield plateau. In the early stage of the holding period, there are more grain boundaries, and there is a greater number of dislocations stacked at the grain boundaries. These dislocations in the tensile process and their accumulation will produce stress concentration. When stress reaches
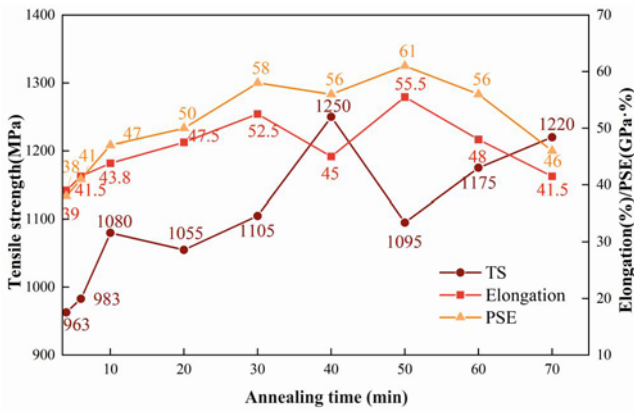
Fig. 10. Mechanical properties of the material for different annealing times.
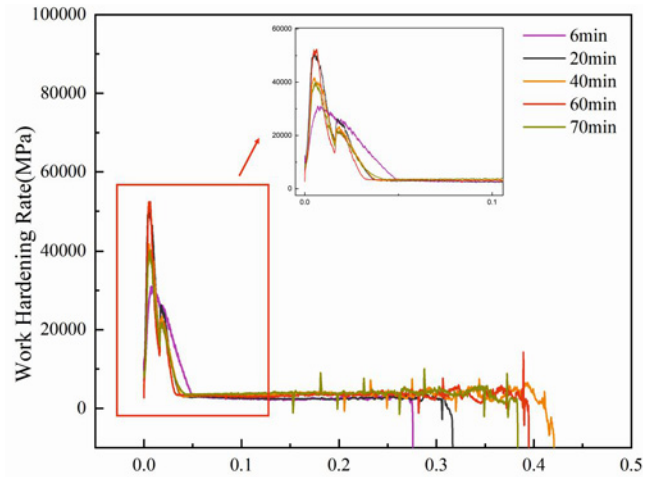

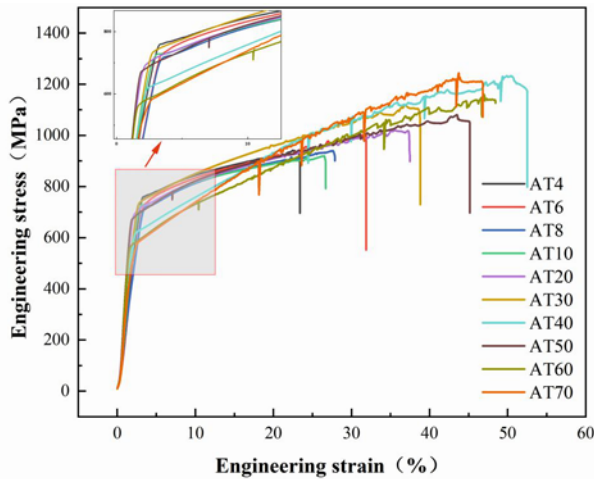Fig. 12. Work hardening curves of test steels.

Fig. 11. Engineering stress-strain curves of test steel.

a critical level, dislocations are generated across grain boundaries, or a new source of dislocations is created at the grain boundaries, so that the stress is relatively stable within a certain strain range, forming a yielding plateau.

However, with the extension of annealing time, the grain begins to grow. During grain growth, the grain boundary area decreases relatively. A smaller grain boundary area means that there are fewer opportunities for dislocations to accumulate and interact at the grain boundary. At the same time, the internal structure of the grown grains is more homogeneous, and there are fewer impediments to dislocation movement. For example, in large grains, dislocations can move in a relatively homogeneous lattice environment and are no longer hindered, as in small grains with many grain boundaries, thereby eliminating the yield plateau [15].

Currently, the elongation and tensile strength are lower. As the annealing temperature increases, the

tensile curve after the section shows pronounced jitter, which may be due to the latter part of the tensile process. Under increasing stress, the austenite phase transformed to martensite. This stress-induced martensite phase transformation is often accompanied by volume expansion. When volume expansion occurs, it is localized within regions of increased compressive stress; these stresses alter the surrounding austenite stress state, thereby increasing the austenite's susceptibility to deformation and phase change. These compressive stresses alter the stress state of the surrounding austenite, thereby increasing its susceptibility to deformation and phase transformation. This mutually reinforcing process of phase transformation and deformation is not uniform and stable. In localized regions, austenite may transform rapidly into martensite, leading to sudden changes in stress and, consequently, oscillatory tensile curves.

Moreover, the degree of initiation and the rate of progression of the martensitic phase transformation may vary across different locations in the material. Due to differences in the internal microstructure of the material, such as grain size, orientation, defect distribution, etc., different regions have different austenite stability. Some regions may undergo phase transformation first, while others lag; this uneven phase transformation leads to fluctuations in tensile force.

From Fig. 12, it can be seen that the work-hardening rate curves under different annealing times show obvious differences, and the effect of annealing time on the work-hardening rate is as follows:

The work-hardening rate increases relatively slowly when strain is small and annealing time is short, whereas it rises slightly faster with longer annealing time. This may be because materials with shorter annealing times exhibit relatively slower proliferation of internal dislocations and other defects during initial
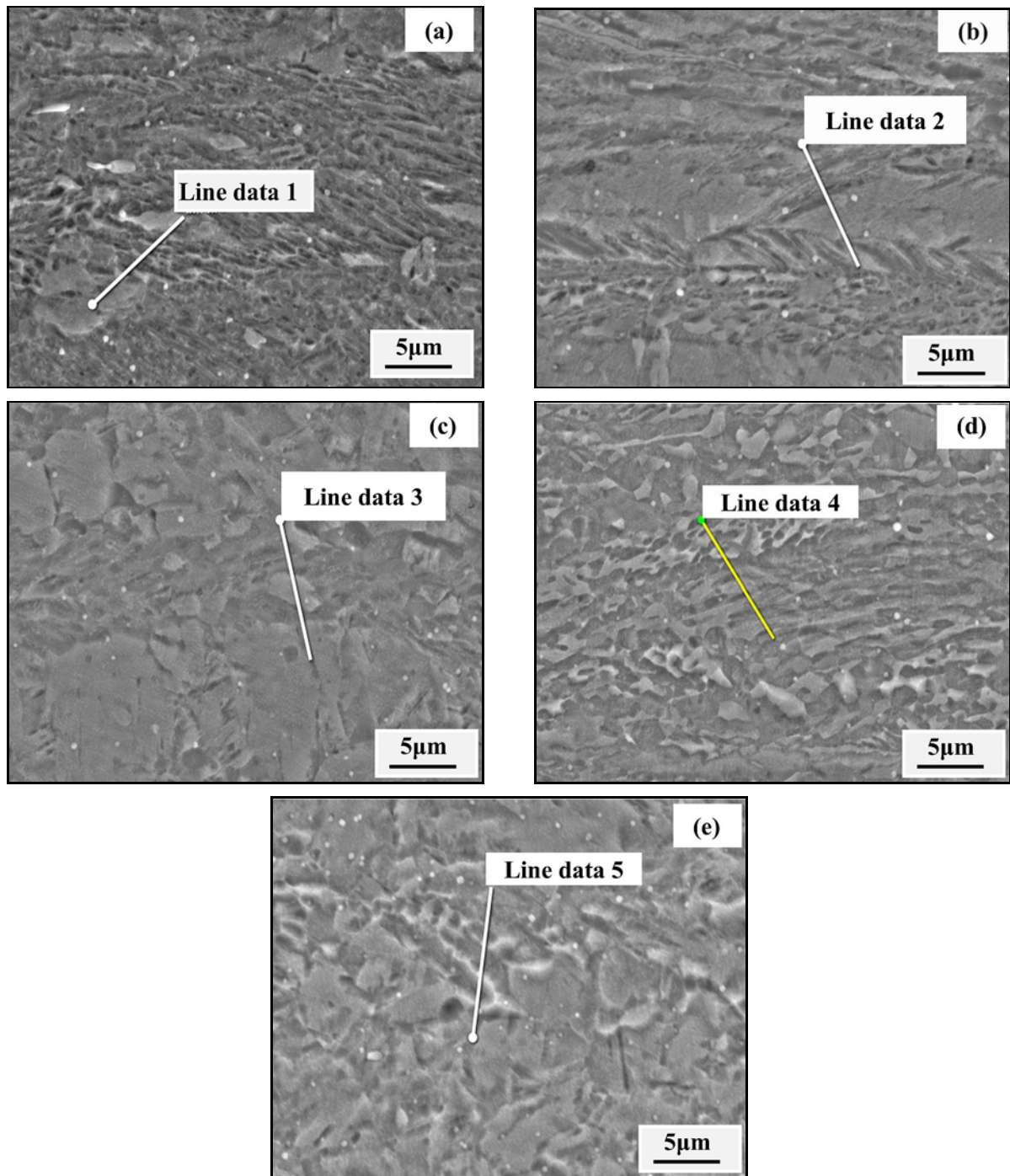
Fig. 13. Line scan images of the material at different annealing times (annealing times of 6, 20, 40, 60, and 70 min for plots (a) to (e), respectively).

deformation, resulting in a lower work-hardening rate [16].

As the true strain increases, each curve reaches a peak. The peak value of the curve with an annealing time of 6 min is the lowest, and the peak value of the curve gradually increases with the extension of annealing time. It indicates that increasing the annealing time can lead to greater work hardening during deformation, thereby improving the material's strength.

After reaching the peak, the work-hardening rate declines. The curve with shorter annealing time decreases more rapidly, while the curve with longer annealing time decreases more slowly. It indicates that the work-hardening capacity of materials with short annealing time declines more rapidly in the late stage of deformation, while materials with long annealing time can maintain a certain work-hardening capacity in a wide range of deformation [17].
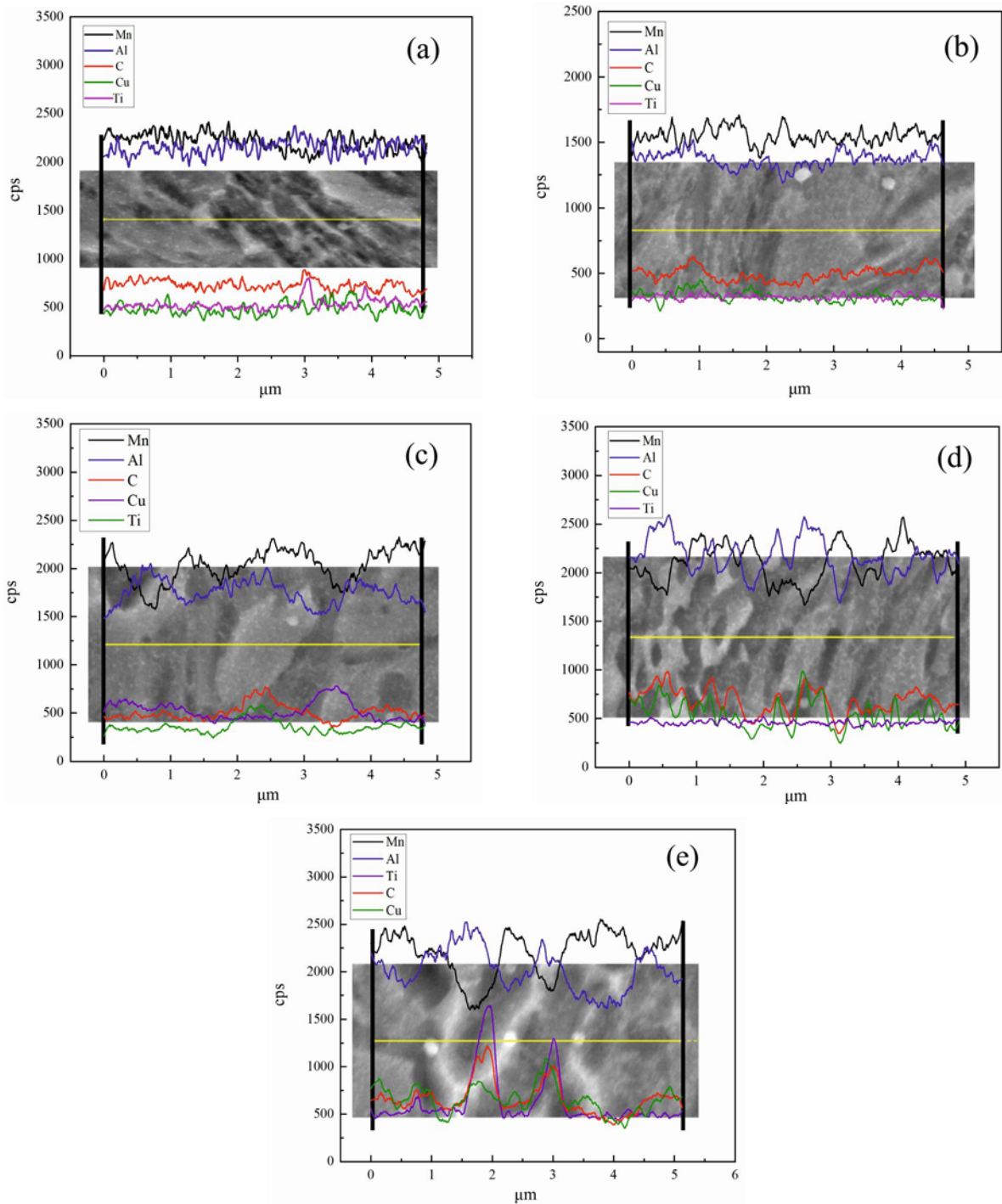
Fig. 14. Line scan and elemental distribution images of the material at different annealing times: (a)–(e) annealing times of 6, 20, 40, 60, and 70 min.

3.3. Elemental distribution analysis

Line scanning was carried out on the test steel using SEM, as shown in Figs. 13 and 14. Figure 13 shows line-scanning images of the material at different annealing times. Figures 13a-e are the line scanning images of annealing times of 6, 20, 40, 60, and 70 min, respectively, and Figs. 14a–e correspond to the elemental distribution of Fig. 13 at the location of the line scanning.

It can be seen that with increasing annealing time, the morphology and size of austenite change significantly, whereas the lower limit of manganese content fluctuation decreases, indicating that manganese did not diffuse at the beginning of the annealing process. Currently, the manganese content in the austenite cen-

ter is high, and with the extension of the annealing time, the manganese element diffuses from the ferrite to the austenite, resulting in a decrease in the lower limit of the fluctuation of its content.

As shown in Fig. 14, the phenomenon of elemental partitioning under different annealing times can be divided into four stages according to the length of annealing time.

The first stage is primarily composed of austenite-shaped nuclei. Due to the significant difference in the C-atom content between ferrite and carburite, the interface between the two is prone to C-atom concentration fluctuations, which in turn lead to structural fluctuations. These local inhomogeneities serve as ideal sites for austenite nucleation.

The second stage is the initial growth of austenite. During this period, carburite continues to decompose, and ferrite gradually transforms into austenite. The difference in the concentration of C atoms between the γ/carburite interface and the α/γ interface induces the diffusion of C atoms within the austenite from the γ/carburite interface to the α/γ interface. This diffusion process disrupts the equilibrium of C concentration at the original interface. In order to maintain the C concentration equilibrium at the interface, carburite can only continue to dissolve into austenite, and ferrite continues to be transformed into austenite, which ultimately promotes the continuous growth of austenite.

The third stage is the completion of austenite growth. At this time, the diffusion of C atoms reaches the subequilibrium state, and the remaining carburite continues to decompose and incorporate into austenite. At this stage, the chemical potential difference between ferrite and Mn and Cu atoms in austenite primarily governs the austenite growth process.

By the fourth stage, homogenization of the austenite composition predominates. In this stage, Mn and Cu atoms continue to diffuse within the austenite until they are uniformly distributed. In summary, during heat retention in the two-phase zone, austenite growth is primarily driven by the diffusive partitioning of C in the early stage, whereas in the late stage it is driven by the diffusive partitioning of Mn and Cu.

Taking Fig. 14c as an example, it can be seen that at this time the austenite morphology is mainly massive, the manganese and aluminum content in the massive austenite region presents a distribution phenomenon of "low aluminum and high manganese", and there exists a phenomenon that the undulation of carbon and manganese is opposite to the undulation of aluminum in the austenite region. It can also be observed that the copper element may be present in the distribution pattern and is very similar to the change in the carbon element. The variation of the element is very similar to that of carbon; in manganese steels, copper atoms are distributed among different phases (e.g., ferrite, austenite). This is due to the limited solubility of copper in steel; when conditions such as steel composition and temperature change, copper atoms tend to segregate or precipitate in certain phases or at grain boundaries.

As shown in Fig. 14e, a second phase of totalization is diffusely distributed throughout the manganese steel microstructure. This high-strength second phase significantly enhances the strength of the material. When strain occurs in the material, it can effectively pin dislocations, impeding their motion and thereby enhancing the material's mechanical properties and providing a stronger guarantee of performance for medium manganese steel in practical applications.

4. Conclusions

(1) When the annealing time was 40 min, the AT40 specimens showed the best mechanical properties with a tensile strength of 1250 MPa, an elongation of 45 %, and a strong plasticity product of up to 56.3 GPa%.

(2) The extension of annealing time drove the specimen grain transformation from fine grains to massive, and the K value calculation yielded that the mechanical stability of residual austenite showed a tendency of decreasing and then increasing with the increase of annealing time.

(3) Changing the annealing time can regulate the distribution of Mn elements, which affects the content and stability of the residual austenite. AT40 specimens with Mn-enriched residual austenite exhibited improved residual-austenite quality and could uniformly sustain martensitic transformation, thereby achieving optimal mechanical properties.

(4) Appropriate dislocation density in austenite improves specimen mechanical properties. AT40 specimens with moderate grain size, moderate dislocation density, and an increased proportion of movable dislocations are strengthened by Hall-Petch, while allowing dislocation slip to coordinate deformation, resulting in improved mechanical properties of the specimens.

References

[1] Y. Sun, J. Zhou, R. Hu, H. Pan, K. Ding, M. Lei, Y. Gao, The high-cycle tensile-shear fatigue properties and failure mechanism of resistance spot-welded advanced high-strength steel with a Zn coating, Materials 17 (2024) 4463.
https://doi.org/10.3390/ma17184463

[2] C. Jing, X. Ding, D. Ye, J. Zhao, T. Lin, S. Xu, Effect of different isothermal time on microstructure and mechanical property of the low-carbon steel treated by dual-stable C-Mn partitioning process, Scanning 2020 (2020) 5931721.
https://doi.org/10.1155/2020/5931721

[3] D. Kumar, S. Sanyal, M. K. Yadav, I. Sen, T. K. Bandyopadhyay, Correlation between intercritical annealing duration and the tensile deformation behavior of Fe-7.5Mn-3.25Al-1Si-0.2C steels: Role of austenite stability, δ-ferrite, and texture, Journal of Alloys and Compounds 1013 (2025) 178506.
https://doi.org/10.1016/j.jallcom.2025.178506

[4] S. Yu, Y. G. Deng, Z. Tao, R. D. K. Misra, Y. P. Yang, Effects of intercritical annealing time on microstructure, tensile properties, and cryogenic toughness of newly designed ultra-low C low Ni medium-Mn steel, Journal of Materials Research and Technology 32 (2024) 1245–1255.
https://doi.org/10.1016/j.jmrt.2024.07.222

[5] Z. Wu, C. Jing, Y. Feng, Z. Li, T. Lin, J. Zhao, Effects of different annealing time on microstructure and mechanical properties of lightweight Al-containing medium-Mn steel, Ironmaking & Steelmaking 50 (2023) 1726–1736.
https://doi.org/10.1080/03019233.2023.2224535

[6] Y. Zou, Y. B. Xu, D. T. Han, Z. P. Hu, R. D. K. Misra, L. F. Cao, H. Song, Combined contribution of Cu-rich precipitates and retained austenite on mechanical properties of a novel low-carbon medium-Mn steel plate, Journal of Materials Science 54 (2019) 3438–3454. https://doi.org/10.1007/s10853-018-3021-x

[7] Y. Zheng, K. Wang, Q. Yang, Y. Lin, L. Zhu, X. Wu, B. Han, B. Wang, D. Zhang, J. Feng, R. Cao, Research on the strengthening mechanism of Nb-Ti microalloyed ultra low carbon IF steel, Journal of Materials Research and Technology 30 (2024) 5785–5803.
https://doi.org/10.1016/j.jmrt.2024.05.028

[8] V. Veis, A. Semenko, M. Voron, A. Tymoshenko, R. Likhatskyi, I. Likhatskyi, Z. Parkhomchuk, Lightweight Fe-Mn-Al-C steels: Current state, manufacturing, and implementation prospects, Steel Research International (2025) 2400904.
https://doi.org/10.1002/srin.202400904

[9] S. Kaar, K. Steineder, R. Schneider, D. Krizan, C. Sommitsch, New Ms-formula for exact microstructural prediction of modern 3rd generation AHSS chemistries, Scripta Materialia 200 (2021) 113923.
https://doi.org/10.1016/j.scriptamat.2021.113923

[10] J. Trzaska, L. A. Dobrzanski, Modelling of CCT diagrams for engineering and constructional steels, Journal of Materials Processing Technology 192 (2007) 504–510.
https://doi.org/10.1016/j.jmatprotec.2007.04.099

[11] S. Zheng, P. Qi, S. Y. Feng, J. Zhao, J. Mu, W. Zhang, Y. Zhang, L. Yin, R. Xu, Effect of bainitic transformation during Bainite Quenching and Tempering (BQT) on the tensile properties of 51CrMnV spring steel, Journal of Materials Engineering and Performance (2025). https://doi.org/10.1007/s11665-025-12103-7

[12] Z. Wu, C. Jing, Y. Feng, Z. Li, T. Lin, J. Zhao, L. Liu, Effect of a new pretreatment-Q&P process on the microstructure and mechanical properties of light-weight Al-containing medium-Mn steels, Materials Science and Engineering: A 862 (2023) 144468.
https://doi.org/10.1016/j.msea.2022.144468

[13] Z. Wang, Q. Yuan, Q. Zhang, S. Liu, G. Xu, Microstructure and mechanical properties of a cold rolled gradient medium-carbon martensitic steel, Acta Metallurgica Sinica 59 (2023) 821–828.
https://doi.org/10.11900/0412.1961.2021.00233

[14] K.-I. Sugimoto, M. Kobayashi, S.-I. Hashimoto, Ductility and strain-induced transformation in a high-strength transformation-induced plasticity-aided dual-phase steel, Metallurgical Transactions A 23 (1992) 3085–3091. https://doi.org/10.1007/BF02646127

[15] S. Kondo, T. Mitsuma, N. Shibata, Y. Ikuhara, Direct observation of individual dislocation interaction processes with grain boundaries, Science Advances 2 (2016) e1501926.
https://doi.org/10.1126/sciadv.1501926

[16] X. Wang, A. Zhao, S. Chen, Z. Bao, Effect of annealing process on microstructure and mechanical property of medium-manganese TRIP steel, International Journal of Materials & Product Technology 64 (2022) 265–277.
https://doi.org/10.1504/IJMPT.2022.122896

[17] X. Yuan, L. Chen, Y. Zhao, H. Di, F. Zhu, Influence of annealing temperature on mechanical properties and microstructures of a high manganese austenitic steel, Journal of Materials Processing Technology 217 (2015) 278–285.
https://doi.org/10.1016/j.jmatprotec.2014.11.027